FRET imaging and statistical signal processing reveal positive and negative feedback loops regulating the morphology of randomly migrating HT-1080 cells

Katsuyuki Kunida[1], Michiyuki Matsuda[1,2] and Kazuhiro Aoki[2,3,*]

[1]Department of Pathology and Biology of Diseases, Graduate School of Medicine, Kyoto University, Sakyo-ku, Kyoto 606-8501, Japan
[2]Laboratory of Bioimaging and Cell Signaling, Graduate School of Biostudies, Kyoto University, Sakyo-ku, Kyoto 606-8501, Japan
[3]PRESTO, Japan Science and Technology Agency (JST), 4-1-8 Honcho Kawaguchi, Saitama 332-0012, Japan
*Author for correspondence (k-aoki@lif.kyoto-u.ac.jp)

Summary

Cell migration plays an important role in many physiological processes. Rho GTPases (Rac1, Cdc42, RhoA) and phosphatidylinositols have been extensively studied in directional cell migration. However, it remains unclear how Rho GTPases and phosphatidylinositols regulate random cell migration in space and time. We have attempted to address this issue using fluorescence resonance energy transfer (FRET) imaging and statistical signal processing. First, we acquired time-lapse images of random migration of HT-1080 fibrosarcoma cells expressing FRET biosensors of Rho GTPases and phosphatidyl inositols. We developed an image-processing algorithm to extract FRET values and velocities at the leading edge of migrating cells. Auto- and cross-correlation analysis suggested the involvement of feedback regulations among Rac1, phosphatidyl inositols and membrane protrusions. To verify the feedback regulations, we employed an acute inhibition of the signaling pathway with pharmaceutical inhibitors. The inhibition of actin polymerization decreased Rac1 activity, indicating the presence of positive feedback from actin polymerization to Rac1. Furthermore, treatment with PI3-kinase inhibitor induced an adaptation of Rac1 activity, i.e. a transient reduction of Rac1 activity followed by recovery to the basal level. In silico modeling that reproduced the adaptation predicted the existence of a negative feedback loop from Rac1 to actin polymerization. Finally, we identified MLCK as the probable controlling factor in the negative feedback. These findings quantitatively demonstrate positive and negative feedback loops that involve actin, Rac1 and MLCK, and account for the ordered patterns of membrane dynamics observed in randomly migrating cells.

Key words: Rac1, FRET, Feedback, Adaptation

Introduction

Cell migration is an essential process in a wide variety of biological phenomena, such as embryonic development, wound repair, immune surveillance, tumor cell invasion and metastasis in mammalian cells (Lauffenburger and Horwitz, 1996). Extracellular cues elicit the various intracellular responses in the organization of both the actin and the microtubule cytoskeletons. It is widely accepted that the major driving force of migration is the extension of a leading edge protrusion or lamellipodium, cell body contraction, and detachment of adhesions at the cell rear (Rajakulendran et al., 2009). All these steps involve the assembly, disassembly and reorganization of the actin cytoskeleton, which are coordinated both in space and time (Mitchison and Cramer, 1996; Rajakulendran et al., 2009).

The molecular mechanisms of cell migration have been extensively studied in tissue culture cells. Rho GTPases and lipid kinases have been identified as key regulators of cell migration. The best-characterized function of Rho GTPases is in the regulation of actin dynamics: RhoA increases the actomyosin contractility, whereas Rac1 and Cdc42 induce the polymerization of actin to form lamellipodial and filopodial protrusions, respectively (Ridley, 2001). Phosphatidyl inositols, which are composed of a D-*myo*-inositol-1-phosphate linked through its phosphate group to diacylglycerol, are phosphorylated and

dephosphorylated by phosphatidyl inositol kinases and phosphatases, generating distinct phosphoinositide species (Saarikangas et al., 2010). Among them, phosphatidylinositol 3,4,5-trisphosphate [$PtdIns(3,4,5)P_3$] and phosphatidylinositol bisphosphates [$PtdIns(3,4)P_2$ and $PtdIns(4,5)P_2$] regulate reorganization of the actin cytoskeleton by providing a membrane-binding platform for a variety of proteins, including guanine nucleotide exchange factors (GEFs) for Rho GTPases and actin filament nucleating proteins (Saarikangas et al., 2010). With the advent of a myriad of fluorescent proteins, genetically encoded biosensors have been increasingly used to visualize the activities of Rho GTPases and phosphatidylinositols (Aoki et al., 2008; Miyawaki, 2003). In particular, live-cell imaging with biosensors based on the principle of Förster (or fluorescence) resonance energy transfer (FRET) have uncovered the spatiotemporal dynamics of these molecules in migrating cells (Itoh et al., 2002; Kurokawa and Matsuda, 2005; Nishioka et al., 2008).

Morphological polarization (i.e. a clear distinction between cell front and rear) is required for cell migration to enable cells to turn intracellularly generated forces into net cell body translocations (Lauffenburger and Horwitz, 1996). It has been suggested that intrinsic mechanisms of intracellular signaling systems with their kinetic fluctuations or noise suffice to activate

this front–rear polarization during the locomotion of eukaryotic motile cells. For example, spatially homogenous stimulation with a chemoattractant, at least for neutrophils, induces a front–rear polarity with a change in filamentous actin (F-actin) distribution from azimuthal symmetry around the cell rim to concentration within a particular region (Coates et al., 1992; Lauffenburger and Horwitz, 1996). In addition, even in the absence of concentration gradients of external stimuli, ordered patterns of cell shape are observed in *Dictyostelium*, flies and mammalian cells, such as directional migration, oscillation behavior of membranes and laterally traveling waves along the cell boundary (Döbereiner et al., 2006; Machacek and Danuser, 2006; Maeda et al., 2008; Weiner et al., 2007). The Turing's reaction–diffusion model is one of the most supported models for the formation of ordered patterns in migrating cells (Gierer and Meinhardt, 1972; Kondo and Miura, 2010; Otsuji et al., 2010). On the basis of a framework in the reaction–diffusion model, self-enhancing positive and negative feedback regulations play a pivotal role in the autonomous emergence of an ordered pattern. It is suggested that PtdIns(3,4,5)P_3, Rac1 and the actin cytoskeleton are part of a positive feedback loop that can initiate polarization (Peyrollier et al., 2000; Srinivasan et al., 2003; Wang et al., 2002; Weiner et al., 2002). However, contrary to these models, rapid activation of endogenous Rac1 proteins triggered effective actin polymerization but failed to activate phosphoinositide 3-kinase (PI3K) to generate PtdIns(3,4,5)P_3 or induce cell polarization (Inoue and Meyer, 2008). Furthermore, the molecular

mechanisms of such negative feedback loops remain largely unknown. We have attempted to identify molecular mechanisms of positive and negative feedback loops underlying the random migration of mammalian cells using FRET imaging with statistical signal processing.

Results

Time-lapse imaging of Rho GTPases, phosphatidylinositols and F-actin in randomly migrating HT-1080 cells

We aimed to elucidate the molecular networks of Rho GTPases and phosphatidylinositols in randomly migrating mammalian cells by time-lapse imaging. We used human HT-1080 fibrosarcoma cells, which exhibit a high motility and invasiveness, as a model system of spontaneous random migration (Hoffman, 2005; Itoh et al., 2002). All experiments presented below employed time-lapse imaging of HT-1080 cells 1 hour after seeding on collagen-coated glass-bottomed dishes to induce spontaneous migration. The HT-1080 cells expressing biosensors were imaged every 1 minute for 2 hours in order to minimize phototoxicity and photobleaching.

We first examined the activity of the Rho GTPases Rac1, Cdc42 and RhoA in migrating HT-1080 cells using the FRET biosensors Raichu–Rac1, Raichu–Cdc42 and Raichu–RhoA, respectively. As reported previously (Itoh et al., 2002; Kraynov et al., 2000; Nalbant et al., 2004), Rac1 and Cdc42 were locally activated at lamellipodia and membrane ruffles at the leading edge, and inactivated at the retracting tail of migrating cells
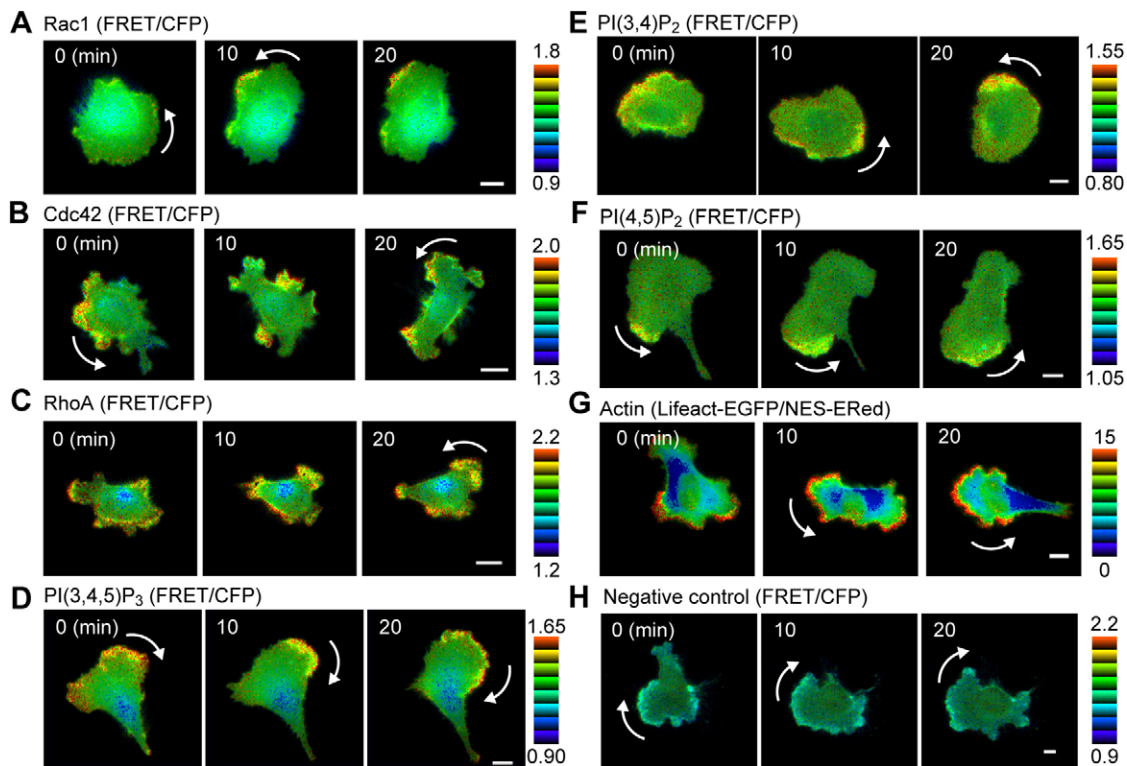

Fig. 1. Spatiotemporal activity maps of signaling molecules in randomly migrating HT-1080 cells. HT-1080 cells transfected with the plasmid encoding the indicated biosensors were imaged for CFP and FRET every 1 minute. FRET/CFP ratio ranges in intensity modulated display (IMD) mode, which associates color hue with emission ratio value and the intensity of each hue with the source image brightness, are shown at the right of each image. Scale bars: 10 μm.
(**A–F,H**) Montage images showing the spontaneous migration of HT-1080 cells expressing the biosensors Raichu–Rac1 (A), Raichu–Cdc42 (B), Raichu–RhoA (C), Pippi–PtdIns(3,4,5)P_3 [PI(3,4,5)P_3], (D), Pippi–PtdIns(3,4)P_2 (E), Pippi–PtdIns(4,5)P_2 (F) and Raichu–PAK–Rho (H). (**G**) Montage images showing the ratio of Lifeact–EGFP to ERed–NES.

(Fig. 1A,B; supplementary material Movies 1, 2). By contrast, activation of RhoA was observed at both the leading edge and retracting tail (Fig. 1C; supplementary material Movie 3). This result was also consistent with the previous findings (Kurokawa and Matsuda, 2005; Pertz et al., 2006).

The spatiotemporal localization of phosphatidylinositols was also visualized with the FRET biosensors (Aoki et al., 2005; Nishioka et al., 2008) Pippi–PtdIns(3,4,5)P_3, Pippi–PtdIns(3,4)P_2 and Pippi–PtdIns(4,5)P_2. PtdIns(3,4,5)P_3 accumulated at the leading edge of migrating HT-1080 cells (Fig. 1D; supplementary material Movie 4), supporting the previous report that PtdIns(3,4,5)P_3 recruits and activates guanine nucleotide exchange factor(s) for Rac1 and Cdc42 (Aoki et al., 2005; Schmidt and Hall, 2002). PtdIns(3,4)P_2 and PtdIns(4,5)P_2 were also found to accumulate at the front of migrating HT-1080 cells (Fig. 1E,F; supplementary material Movies 5, 6). The increase in PtdIns(3,4)P_2 and PtdIns(4,5)P_2 at the lamellipodia of migrating cells could be attributed to the rapid turnover of these lipids (Nishioka et al., 2008).

We also examined the accumulation of F-actin in HT-1080 cells with Lifeact–EGFP, a marker of F-actin (Riedl et al., 2008). To correctly evaluate the accumulation of F-actin at membrane ruffles and pseudopodia (Dewitt et al., 2009), DsRed-express fused with a nuclear export sequence (ERed–NES) was coexpressed with Lifeact–EGFP, and used as a reference of the volume of cytoplasm. There was a higher ratio of Lifeact–EGFP signal to ERed–NES signal at the leading edge of migrating cells, clearly indicating the actin polymerization (Fig. 1G; supplementary material Movie 7). Notably, a negative control of the FRET biosensor, which included a Cdc42- and Rac1-interacting binding (CRIB) domain of PAK1 and RhoA, did not show any spatial or temporal change of FRET signal in HT-1080 cells (Fig. 1H).

Of note, lateral propagation of membrane protrusions and retractions were frequently observed around the cell periphery of migrating HT-1080 cells (Fig. 1, arrows), suggesting that common mechanisms underlie the ordered pattern of membrane dynamics, as observed in the migration of other eukaryotic cells (Döbereiner et al., 2006; Machacek and Danuser, 2006; Maeda et al., 2008).

Quantification of morphological dynamics by auto-correlation analysis

To quantitatively evaluate the morphological changes, the edge velocity of membrane displacement was quantified at the whole cell periphery by a modified mechanical model (Machacek and Danuser, 2006). Briefly, the distance between a window on the cell periphery at time T and that at time $T+1$ was measured using time-lapse images (Fig. 2A,B; supplementary material Fig. S1). Then, the edge velocity was calculated and represented in a heat map as a function of the time and the sampling window around the cell periphery (see Materials and Methods for details; Fig. 2C). Although there was apparent heterogeneity of the pattern in the edge velocity map between different migrating HT-1080 cells, we often recognized a periodic pattern, as shown in Fig. 2C. In almost all cases, migrating cells exhibited one protrusion and one retracting tail, indicating the acquisition of front–back polarity even in the absence of a concentration gradient of external stimuli.

We next classified the migration pattern of HT-1080 cells by applying auto-correlation analysis to the edge velocity map (Döbereiner et al., 2006; Maeda et al., 2008). The auto-

correlation function (ACF) in Fig. 2D has a wave-like pattern, demonstrating the occurrence of the lateral membrane wave along the cell boundary. With the temporal ACF (ΔWindow no.$=0$, dashed line in Fig. 2D), three parameters, Δt_0, Δt_{min} and Δt_{max}, were defined as shown in Fig. 2E. The pattern of the ACF map and threshold criteria of Δt_0 value ($\Delta t_0 > 30$ min) were utilized to classify the pattern of morphological dynamics into four categories: wave-like, oscillatory, directional, and non-classifiable mode (Maeda et al., 2008) (see Materials and Methods for more details; Fig. 2F; supplementary material Movie 8). Almost half of HT-1080 cells demonstrated the wave-like mode of migration (Table 1). Furthermore, the velocity of the lateral membrane wave, V_L, was calculated as 4.2 ± 2.1 μm/minute by dividing the length of the cell periphery by Δt_{max}. These results suggested the existence of an intrinsic signaling network that established an ordered pattern of morphological dynamics without external stimuli. Notably, the expression of FRET biosensors per se did not substantially perturb the mode of cell migration in HT-1080 cells (supplementary material Fig. S2). Therefore, in the following study, we examined a molecular mechanism for generating wave-like motion in randomly migrating HT-1080 cells.

Quantification of correlation and time delay between morphological change and signaling by cross-correlation analysis

To identify a hierarchical connection among Rho GTPases, phosphatidyl inositols and morphological change, we used a cross-correlation analysis and characterized their temporal correlation (Machacek et al., 2009; Tsukada et al., 2008). The cross-correlation function (CCF) between edge velocity (Fig. 3A) and Rac1 activity (Fig. 3B) was calculated with Rac1 activity being fixed as described in the Materials and Methods (Fig. 3C). Temporal CCF was also extracted (Fig. 3C, dotted line) to analyze the lag time of signaling and morphological change (Fig. 3D; supplementary material Fig. S3; Table S1).

The positive peak value of the cross correlation coefficient was obtained with a time delay of -2.2 minutes [95% confidence interval (CI), -3.0 to -1.4 minutes] from Rac1 activity, indicating that the edge velocity was increased before the increase in Rac1 activity and vice versa (Fig. 3E). However, taking the interval of image acquisition (every 1 minute) into account, the Cdc42 activity was slightly delayed or nearly synchronized with morphological change (time delay of -1.3 minutes, 95% CI, -2.2 to -0.5 minutes; supplementary material Fig. S4A). RhoA activity did not demonstrate any correlation with edge velocity (peak value of 0.082; supplementary material Fig. S4B). This was probably because the high RhoA activity at both protrusion and retraction during cell migration marginally contributed to the overall correlation, leading to an offset of the net correlation coefficient value (Kurokawa and Matsuda, 2005). Furthermore, F-actin accumulation was coupled to the edge velocity with a time delay of -0.25 minutes (95% CI, -1.5 to 1.0 minute; Fig. 3F). We time-lapse imaged Rac1 activity and F-actin accumulation every 30 seconds in migrating HT-1080 cells, demonstrating the time delay values of -2.6 minutes (95% CI, -3.3 to -1.5 minutes) and -0.9 minutes (95% CI, -1.4 to -0.4 minutes) for Rac1 activity and F-actin, respectively (supplementary material Fig. S5, Table S1). These values are consistent with those obtained by imaging with the time interval
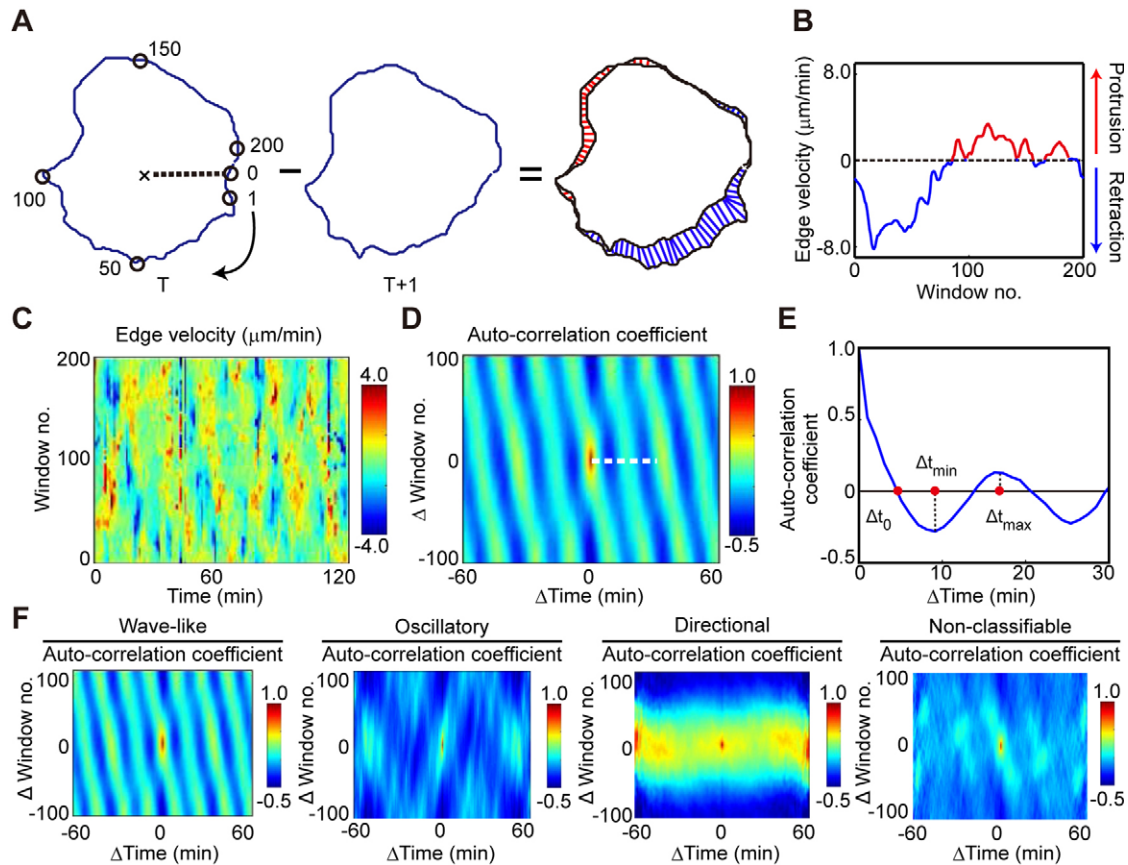
Fig. 2. **Quantification of morphological dynamics by auto-correlation analysis.** (**A**) Left and middle panels show the cell boundaries extracted by image processing at the time *T* and *T*+1, respectively. The window with the angle of 0 in the polar display is defined as an initial window. The right panel shows the merged cell boundary with edge velocity (see Materials and Methods; supplementary material Fig. S1). Red and blue lines represent the positive and negative velocity at each window, respectively. (**B**) Edge velocities are plotted as a function of the window number between the frame *T* and frame *T*+1 (A, left and right panels, respectively). (**C**) Edge velocity is represented as a function of the sampling windows and time. Red and blue indicate protrusion and retraction, respectively. (**D**) The auto-correlation function of the edge velocity map is shown as a function of the shift of the sampling window (ΔWindow no.) and the shift of time (ΔTime). (**E**) The temporal auto-correlation function (ΔWindow no.=0, dotted line in D) is plotted as a function of ΔTime. Δt_0, $\Delta t_{minutes}$ and Δt_{max} are shown as red dots (see Results). (**F**) Representative heat maps of auto-correlation coefficients, which were classified into wave-like, oscillatory, directional and non-classifiable migrations, are shown as a function of ΔWindow no. and ΔTime.

of 1 minute. Of note, we previously demonstrated that EGF-induced Rac1 activation preceded the lamellipodial extension in Cos1 cells (Kurokawa et al., 2004). Thus, the role of Rac1 appears to be different in growth factor-induced and stochastic membrane protrusions.

Cross-correlation analysis revealed that PtdIns(3,4,5)P_3 accumulation was almost synchronized with membrane protrusion (time delay of −1.1 minutes, 95% CI, −1.8 to −0.5 minutes; Fig. 3G). The downstream metabolite, PtdIns(3,4)P_2, demonstrated a time delay of −1.6 minutes in comparison with the edge velocity (95% CI, −2.3 to −0.8 minutes; supplementary material Fig. S4C). PtdIns(4,5)P_2 accumulation was delayed 1.4 minutes (95% CI, −2.0 to −0.7 minutes; supplementary material Fig. S4D). In migrating MDCK cells, phosphatidyl inositol 5-kinase and PLC-γ, but not PI3K, mainly contribute to the distribution of PtdIns(4,5)P_2 at

Table 1. Classification of migration mode based on the auto-correlation analysis

	Wave-like	Oscillatory	Directional	Unclassifiable
Percent (%)	42	6	32	20
Length (μm)	124±35.4	126±23.9	126±31.7	129±23.1
Δt_0 (minute)	10.7±7.54	16.8±8.6	48±22.1	39.6±36.6
Δt_{min} (minute)	19.9±14.8	14.3±3.2	–	–
Δt_{max} (minute)	39.8±24.9	29.0±9.8	–	–
V_L (μm/minute)	4.2±2.1	4.4±1.0	–	–

More than forty cells were analyzed and classified as described in Materials and Methods. Values are means ± s.d.
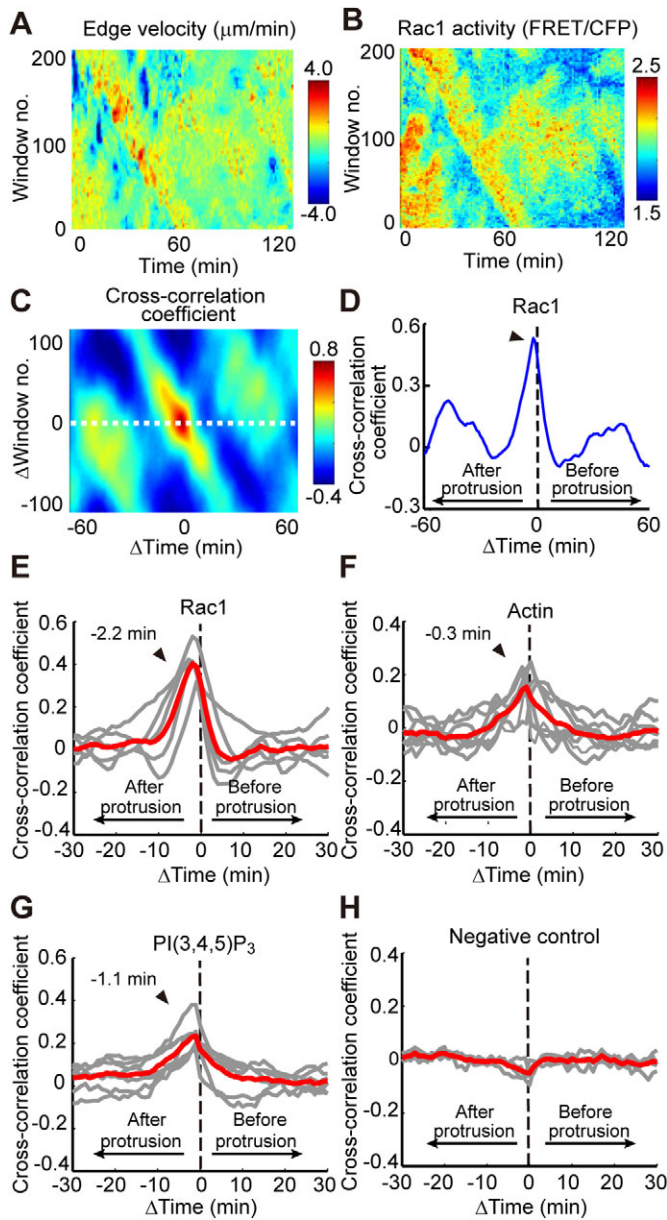
Fig. 3. Quantification of the dynamics between morphological change and signaling molecules by cross-correlation analysis. (**A**,**B**) Edge velocity (A) and Rac1 activity, i.e. the FRET/CFP ratio value (B), are represented as a function of the sampling windows and time. (**C**) The cross-correlation function between edge velocity and Rac1 activity is represented as a function of ΔWindow no. and ΔTime. The edge velocity map was shifted to obtain the cross-correlation function. (**D**) The temporal cross-correlation function (ΔWindow no.=0, dotted line in C) is plotted as a function of ΔTime. The maximum value of the temporal cross-correlation coefficient is obtained at a time lag of −2 minutes from Rac1 activation (arrowhead), indicating that membrane protrusion is initiated 2 minutes before Rac1 activation. (**E–H**) The temporal cross-correlations between edge velocity and Rac1 activity (E), F-actin (F), PtdIns(3,4,5)P_3, (G) and a negative control (H) are shown for individual cells (gray lines). Red lines indicate the average temporal cross-correlation function; $n=6$ (Rac1), $n=8$ (F-actin), $n=7$ [PtdIns(3,4,5)P_3] and $n=5$ (negative control). See supplementary material Fig. S3 and Table S1 for the details.

lamellipodia of the leading edge, suggesting a possible role of phosphatidyl inositol 5-kinase and PLC-γ in random migration in HT-1080 cells (Nishioka et al., 2008). As expected, the negative

control FRET biosensor did not show any direct correlation with edge velocity (Fig. 3H).

In brief, the cross-correlation analysis showed a sequential relationship between signaling molecules and morphological change in the following temporal order: (1) PtdIns(3,4,5)P_3 accumulation and morphological change (polymerized actin localization); (2) PtdIns(3,4)P_2 accumulation and Cdc42 activation; and (3) Rac1 activation.

Perturbation analysis of the signaling pathway

Rac1 induces actin reorganization and, consequently, lamellipodial formation (Hall, 1998). According to this scheme, the delay in Rac1 activation shown in Fig. 3 implies a positive feedback regulation from actin polymerization to Rac1 in migrating HT-1080 cells. To explore this assumption, we examined the effects of the F-actin depolymerizers latrunculin B and cytochalasin D on PtdIns(3,4,5)P_3 accumulation and Rac1 activity. Latrunculin B (Fig. 4A,B) and cytochalasin D (supplementary material Fig. S6A,B) treatment did not induce any change in the level of PtdIns(3,4,5)P_3, but were associated with a decrease in Rac1 activity (Fig. 4C,D). These results indicated that actin polymerization activated Rac1 by a positive feedback mechanism. Cdc42 activity was not suppressed by latrunculin B or cytochalasin D treatment (data not shown), although the reason for this remains unknown. Therefore, we focused on only Rac1 activity in the following study. Next, we investigated another positive feedback mechanism from Rac1 to PI3K (Aoki et al., 2007; Weiner et al., 2002) by the inducible translocation technique (Inoue et al., 2005). Rapamycin triggers heterodimerization formation of a Lyn N-terminal sequence-tagged FRB (LDR) with an FKBP-fused protein. Upon rapamycin treatment, FKBP–Tiam1 was translocated to the plasma membrane, and consequently activated Rac1 within 2 minutes, followed by the formation of lamellipodia (Fig. 4E,G). However, rapid activation of Rac1 did not increase the level of PtdIns(3,4,5)P_3 (Fig. 4F,H). These findings demonstrated that the positive feedback pathway consisting of Rac1 and PI3K did not contribute to the signaling network in migrating HT-1080 cells as reported in HL-60 neutrophils (Inoue and Meyer, 2008).

The results of auto-correlation analysis, which showed a wave-like pattern of membrane dynamics, prompted us to investigate a negative feedback loop involving Rac1, phosphatidyl inositols and morphological change. We found that treatment with a PI3K inhibitor, LY294002, induced an immediate and transient decrease in Rac1 activity to below the basal level, and suppressed lamellipodial protrusions (Fig. 4J,L). Interestingly, Rac1 activity and the morphological repression returned to the basal levels within 20 minutes even though PtdIns(3,4,5)P_3 was sustained at low levels for at least 30 minutes after treatment with LY294002 (Fig. 4I,K). We confirmed these findings using another PI3K inhibitor, PIK-93 (Knight et al., 2006) (supplementary material Fig. S6C,D).

Prediction of a network topology consisting of PI3K, Rac1 and F-actin

The transient suppression of Rac1 by PI3K inhibition might be caused by adaptation, i.e. the ability of the signaling network to reset itself after responding to a stimulus. A recent study revealed that an adaptation emerges from only two major topologies of a
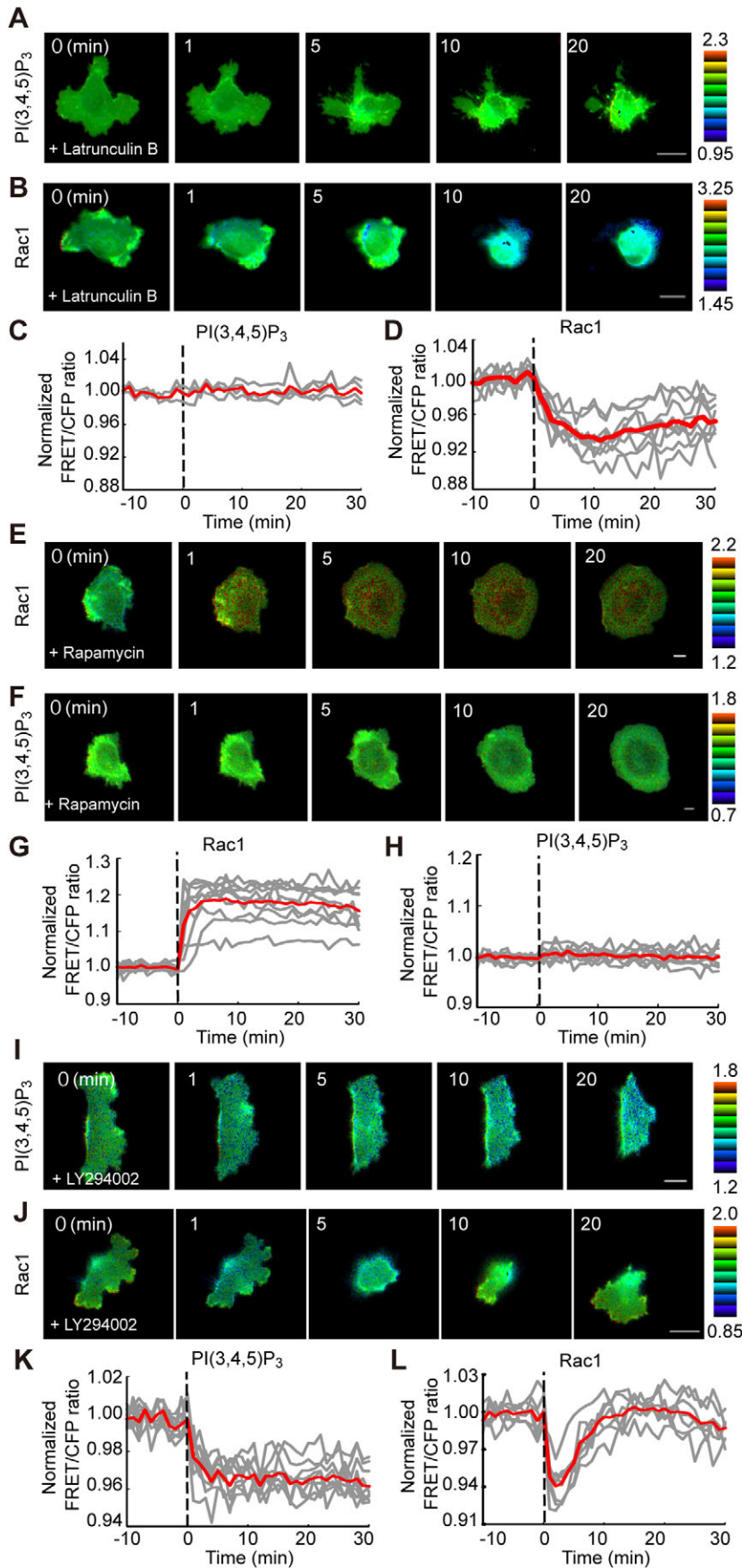
Fig. 4. Perturbation analysis of PI3K–Rac1–Actin signaling by chemical inhibitors. (**A–D**) HT-1080 cells expressing Pippi–PtdIns(3,4,5)P_3 (A) or Raichu–Rac1 (B) were treated with 100 nM latrunculin B, and imaged every 1 minute. FRET images at the indicated time points after latrunculin B addition are shown in IMD mode. Ratio ranges in IMD mode are shown at the right of each image. Scale bars: 10 μm. (C,D) FRET/CFP ratios of Pippi–PtdIns(3,4,5)P_3 (C) and Raichu–Rac1 (D) for the individual cells (gray lines) were expressed by measuring the increase over the basal activity, which was averaged over 10 minutes before latrunculin B addition. Red lines indicate the average FRET/CFP ratio; $n=4$ (C), $n=9$ (D). (**E–H**) HT-1080 cells expressing LDR and FKBP–Tiam1 with Raichu–Rac1 (E) and Pippi–PtdIns(3,4,5)P_3 (F) were treated with 100 nM rapamycin, and imaged every 1 minute. FRET images are shown in E and F. Scale bar: 10 μm. (G,H) FRET/CFP ratios of Raichu–Rac1 (G) and Pippi–PtdIns(3,4,5)P_3 (H) for the individual cells (gray lines) and their average (red) are shown as described for C and D; $n=10$ (G), $n=7$ (H). (**I–L**) HT-1080 cells expressing Raichu–Rac1 (I) and Pippi–PtdIns(3,4,5)P_3 (J) were treated with 20 μM LY294002, and imaged every 1 minute. FRET images are shown in I and J. Scale bars: 10 μm. (K,L) FRET/CFP ratios of Raichu–Rac1 (K) and Pippi–PtdIns(3,4,5)P_3 (L) for the individual cells (gray lines) and their average (red lines) are shown as described for C and D; $n=9$ (K), $n=10$ (L).

signaling network: a negative feedback loop with a buffering node and an incoherent feed forward loop with a proportioner node (Ma et al., 2009). This prompted us to explore possible kinetic models of PI3K, Rac1 and actin polymerization modules by considering the following two constraints: (1) the inhibition of actin polymerization induces a sustained decrease in Rac1 activity, and (2) Rac1 activity and actin polymerization adapt to PI3K inhibition. Because Rac1 activation did not affect PI3K, we set PI3K as an input. Actin polymerization was set as an output for the membrane protrusion. In preliminary simulations, Rac1 was located between PI3K and actin polymerization (supplementary material Fig. S7). None of the models derived from this topology could fulfill the aforementioned constraints because actin polymerization cannot positively regulate Rac1.

Therefore, four models of possible networks with an additional 'node' were constructed to reproduce the experimental results obtained by cross-correlation and perturbation analyses (Fig. 5A). In these models, we assumed that actin polymerization corresponded to the edge velocity. The numerical simulation in every proposed model reproduced the effect of actin polymerization inhibitors and PI3K inhibitors on the change in Rac1 activity – namely, sustained decrease and adaptation, respectively (Fig. 5B, Model A; supplementary material Figs S8–S10 Models B–D, Tables S2–S5).

Role of MLCK as a buffering node among PI3K, F-actin and Rac1 signaling modules

To distinguish these four models, we searched for candidate molecules that might act as nodes in the signaling scheme. In particular, we focused on negative regulators for actin reorganization and Rac1 signaling, and found that myosin light chain kinase (MLCK) and/or its target signaling played a role in a buffering node of the network. To visualize MLCK accumulation, the high molecular mass isoform of human MLCK1 tagged with GFP at the N-terminus, hereafter referred to as EGFP–Long-MLCK, was expressed in HT-1080 cells (Poperechnaya et al., 2000). EGFP–Long-MLCK demonstrated clear accumulation at not only the retracting tail, but also the leading edge of migrating HT-1080 cells (Fig. 6A; supplementary material Movie 9). The temporal CCF demonstrated a positive peak of correlation efficiency at the time delay of approximately −4.0 minutes (95% CI, −4.9 to −3.1 minutes; Fig. 6B, arrow). Furthermore, the negative correlation coefficient peak was obtained at the positive time delay of approximately 0.5 minutes (95% CI, −0.8 to 1.8 minutes; Fig. 6B, arrowhead). These delay timing values did not correlate with the expression level of EGFP–Long-MLCK, negating the artificial effect of over-expression of Long-MLCK on the migration in HT-1080 cells (supplementary material Fig. S11). To validate the relationship between MLCK and Rac1, we examined whether rapid activation of Rac1 induced translocation of MLCK to the periphery of the membrane. As expected, rapamycin-induced heterodimerization between LDR and FKBP–Tiam1-activated Rac1, which in turn increased the level of localization of EGFP–Long-MLCK at the peripheral membrane (Fig. 6C, arrows) with a delay of 4.6 minutes (Fig. 6D). In addition, treatment with an MLCK inhibitor, ML-7, induced a rapid increase in Rac1 activity (Fig. 6E,F). Thus, a reaction between Rac1 and MLCK could be the buffering node, which was postulated in Model A (Fig. 5). Finally, we examined the involvement of Rho-associated protein kinase (ROCK), which is well known to regulate myosin contractility (Totsukawa et al.,
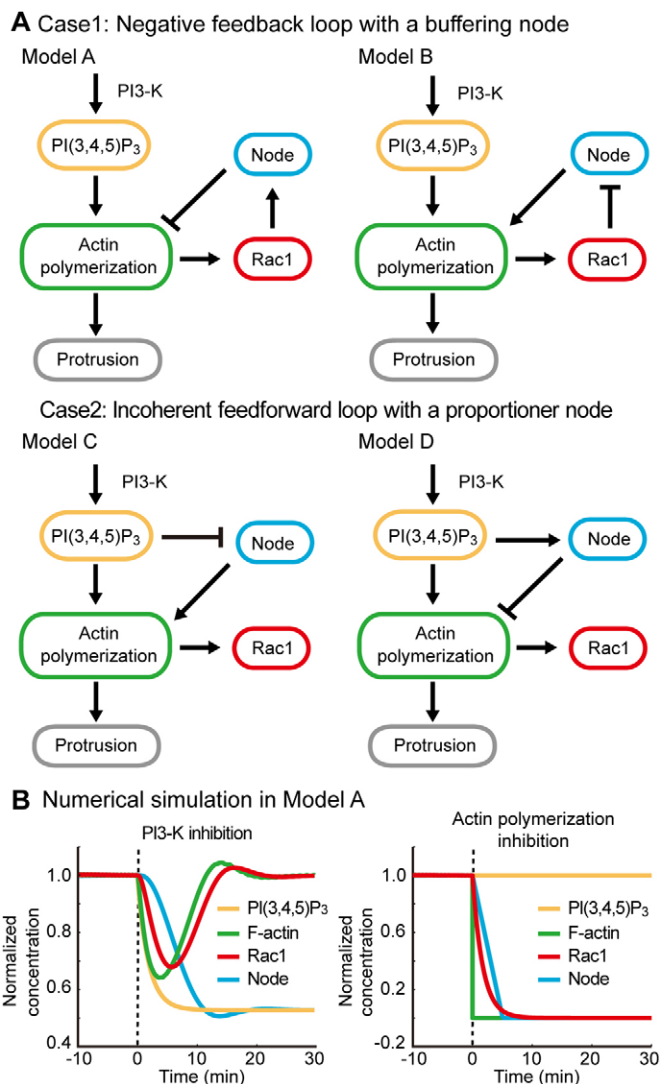

Fig. 5. In silico modeling and simulation of PI3K–Rac1–Actin signaling. (**A**) On the basis of the results in Fig. 4C,D,K,L, four possible models were considered. Model A and Model B included a negative feedback loop with a buffering node (case 1). Model C and Model D included an incoherent feedforward loop with a proportioner node (case 2). All these models assume the existence of a hypothetical 'node' molecule. (**B**) Ordinary differential equations in Model A were described by the Michaelis–Menten scheme, and numerically solved. Left and right graphs show the time course of PtdIns(3,4,5)P_3 (orange), F-actin (green), Rac1 (red), and node (blue) as a function of time after inhibition of PI3K and inhibition of actin polymerization, respectively. PI3K inhibition results in a 90% reduction of the PI3K level at time 0. However, inhibition of actin polymerization reduces the F-actin level to 0 at time 0. All reactions and parameters are shown in supplementary material Tables S2–S5.

2004). ROCK inhibitor, Y27632, was added to the medium of HT-1080 cells expressing Raichu–Rac1 to determine whether Y27632 increased Rac1 activity as ML-7 does. Unexpectedly, however, Y27632 had little effect on Rac1 activity, although Y27632 induced typical morphological changes in ROCK inhibition: long protrusions and a sickle-cell shape (supplementary material Fig. S12). These results strongly supported the negative feedback loop in Model A, in which the MLCK pathway acted as a buffering node for the negative feedback.
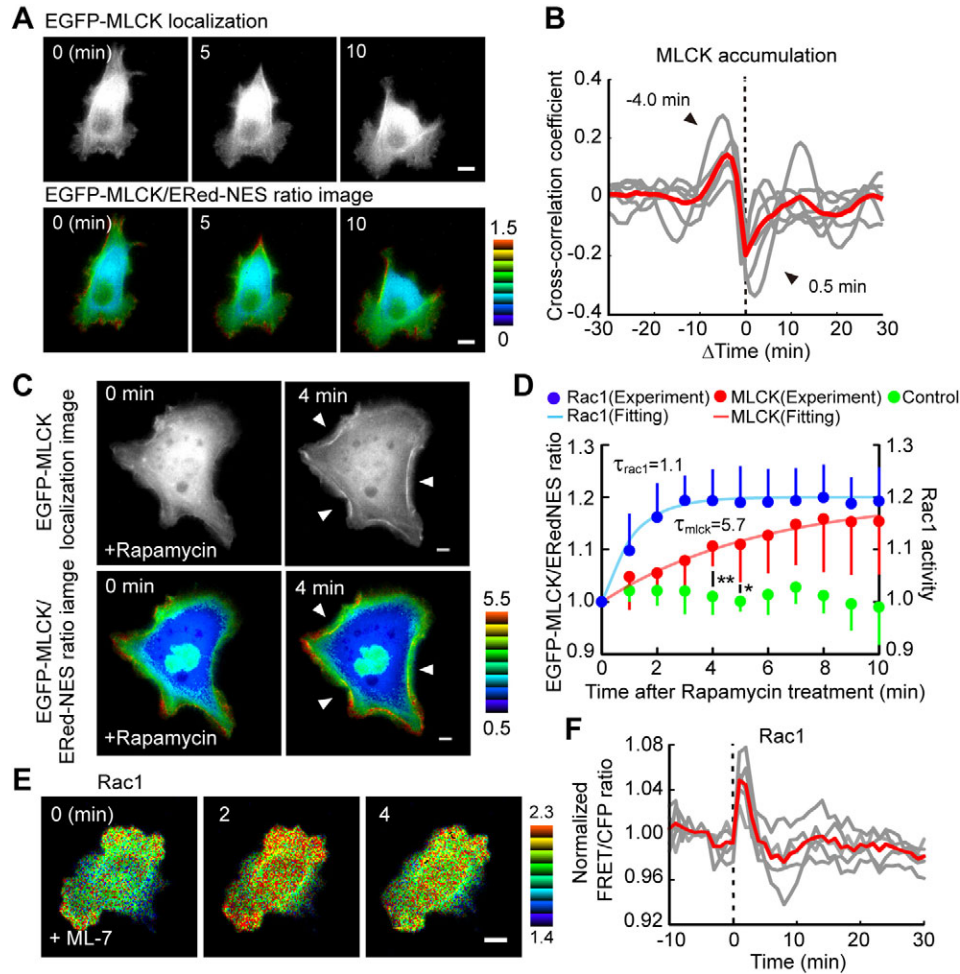
Fig. 6. Identification of MLCK as a buffering node of the negative feedback loop. (**A**) HT-1080 cells expressing the long isoform of MLCK fused with EGFP (EGFP–Long-MLCK) and ERed-NES as a cytoplasmic reference were imaged every 1 minute. EGFP and ratio images at the indicated time points are shown. Ratio ranges in IMD mode are shown at the right of each image. Scale bars: 10 μm. (**B**) Temporal cross-correlation between edge velocity and Long-MLCK localization are shown for individual cells (gray lines). The red line indicates average temporal cross-correlation function; $n=6$. (**C,D**) HT-1080 cells expressing LDR and FKBP–Tiam1 with EGFP–Long-MLCK and ERed-NES were treated with 100 nM rapamycin, and imaged every 1 minute. The ratio images are shown in C. Arrowheads indicate the accumulation of EGFP–Long-MLCK after rapamycin treatment. Scale bars: 10 μm. (D) The mean EGFP–MLCK/ERed-NES ratios at the cell periphery (red and green circles) and the FRET/CFP ratios of Raichu–Rac1 over the whole cell (blue circles) from measurements of the relative increase compared with the reference value at 0 minutes of rapamycin addition. FKBP–Tiam1 and FKBP were used as Rac1 activator (blue and red) and control (green), respectively. Blue and red lines are the curves fitted with a single exponential function, and τ_{rac1} and τ_{mlck} are their time constants. Bars represent the standard deviation; $n=5$ (Rac1), $n=6$ (MLCK) and $n=5$ (control). (**E,F**) HT-1080 cells expressing Raichu–Rac1 were treated with 20 μM ML-7, an MLCK inhibitor, and imaged every 1 minute. FRET images are shown in Fig. 1A. Scale bar: 10 μm. (F) FRET/CFP ratios of Raichu–Rac1 for the individual cells (gray lines) and their average (red line) are shown as described in Fig. 4D ($n=5$).

Discussion

In this study, we have revealed a signaling network comprising positive and negative feedback regulations between PI3K, actin polymerization, Rac1 and MLCK in randomly migrating HT-1080 cells (Fig. 7A). On the basis of the auto- and cross-correlation analyses, we can summarize the relative delay timing in comparison to edge velocity change (Fig. 7B) and the process of signaling and membrane protrusion and retraction as follows (Fig. 7C). In the first phase of protrusion, the edge velocity takes a positive value, indicating membrane extension and actin polymerization (0 minutes). Simultaneously or slightly after membrane protrusion, PtdIns(3,4,5)P_3 accumulates at the tip of the protrusion. In the second phase, after the initiation of membrane extension (2 minutes), Rac1 activity increases. In the

third phase (4 minutes), MLCK accumulates at the tip of the leading edge in a Rac1-dependent manner, and consequently decelerates the edge velocity through actin reorganization. According to the results of the auto-correlation analysis, the lateral membrane wave revolves around the cell periphery with a periodicity of 40 minutes. Thus, the edge velocity, Rac1 activity and MLCK localization reach a peak at 10, 12 and 14 minutes, respectively. Meanwhile, the edge position of the cell periphery is described by integrating the edge velocity value, and peaks at 20 minutes after the start of the increase in edge velocity (Fig. 7C, gray line). The latter half of the process, i.e. retraction, represents the same sequential process in which the edge velocity and molecular activities show negative and low values, respectively.
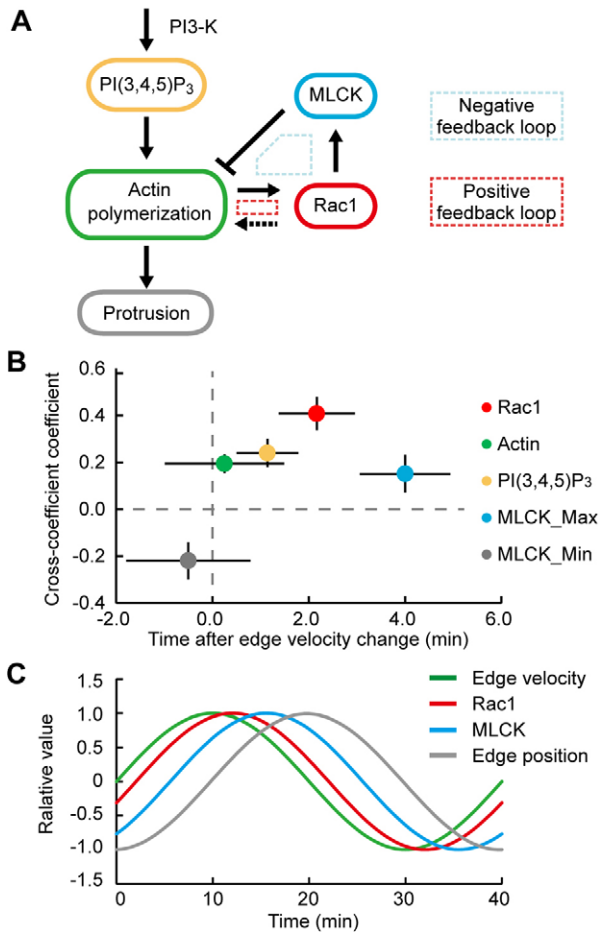
Fig. 7. Signaling network in randomly migrating HT-1080 cells. (**A**) A schematic representation of the signaling network between PI3K, actin polymerization, Rac1 and MLCK. Negative and positive feedback loops are indicated as blue and red dashed boxes, respectively. (**B**) Cross-correlation coefficients of Rac1, F-actin, PtdIns(3,4,5)P_3 and MLCK (maximum and minimum) are plotted as a function of relative timing from edge velocity change. Bars represent 95% confidence intervals. (**C**) The sequential order of edge velocity (actin polymerization), Rac1, MLCK and edge position are shown as a function of time. The edge position of the cell periphery was obtained by integrating the edge velocity value. The time shifts of Rac1 and MLCK from edge velocity are 2 minutes and 5.5 minutes, respectively. On the basis of the results of auto-correlation analysis, the lateral membrane wave revolves around the cell periphery with a periodicity of 40 minutes.

We propose that a reaction–diffusion system of the signaling network generates the lateral propagation of waves around the cell periphery (Kondo and Miura, 2010). The positive feedback loop from Rac1 to actin polymerization amplifies the increase in the edge velocity and the lamellipodial protrusion. This actin polymerization signal diffuses laterally along the cell periphery. Meanwhile, the negative feedback loop comprising MLCK as a buffering node and Rac1 as the input, respectively, retracts the membrane with a time delay. Consistent with this idea, Otsuji et al. have reported a mass-conserved reaction diffusion with positive and negative feedback loops, which reproduces characteristic behaviors of membrane dynamics, including lateral wave propagation (Otsuji et al., 2010). Our data provide a molecular basis for their mathematical modeling. Furthermore, Arai et al. have found that self-organized waves of

PtdIns(3,4,5)P_3 are generated spontaneously on the membrane of *Dictyostelium* cells in the presence of latrunculin A, and they have developed a reaction diffusion model that recapitulates the relaxation oscillator of phosphatidylinositol dynamics with positive and negative feedback loops (Arai et al., 2010). This model differs from the present models of HT-1080 cells in terms of the signaling hubs: phosphatidylinositols play a central role in the positive and negative regulations in *Dictyostelium* cells, whereas Rac1 acts as a signaling hub for two feedback loops, as observed in HT-1080 cells. Of note, the velocity of the lateral membrane wave in this study, ~4 μm/minutes (Table 1), was comparable with those in mouse embryonic fibroblasts (2.4 μm/minutes), fly cells (0.72 μm/minutes), T cells (0.33 μm/minutes) (Döbereiner et al., 2006) and *Dictyostelium* cells (2–4 μm/minutes as roughly calculated from Arai et al. (Arai et al., 2010), implying the presence of general molecular mechanisms underlying the random migration of eukaryotic cells.

One of the key findings in this study was that a negative feedback loop from Rac1 to MLCK enables the system of actin reorganization to adapt to external perturbations. We assumed that GTP–Rac1 recruits MLCK to the edge of membrane protrusions either directly or indirectly, leading to the retraction of the peripheral plasma membrane by increasing the actomyosin contractility. Consistent with this model, MLCK localizes at the leading edge of lamellipodia in mouse embryonic fibroblasts, and regulates the periodic lamellipodial contractions (Giannone et al., 2004). The long MLCK directly binds to actin filaments in vitro and in interphase cells, and these bindings are mediated by five DXRXXL motifs (Poperechnaya et al., 2000; Smith et al., 2002). The inhibition of ROCK by Y27632 did not alter Rac1 activity (supplementary material Fig. S12), suggesting two possible molecular mechanisms of the negative feedback. First, the negative feedback from MLCK to Rac1 was mediated through myosin that was regulated by MLCK, but not ROCK. There are many reports showing spatial and functional discrepancies of myosin regulations between MLCK and ROCK (Totsukawa et al., 2004). Second, myosin-independent MLCK activity mediates the negative feedback from MLCK to Rac1. Consistent with this hypothesis, myosin-independent effect of MLCK on migration of mammalian cells has been reported (Kudryashov et al., 1999; Niggli et al., 2006). In disagreement with the negative feedback model, the rapid and global activation of Rac1 by FKBP–Tiam1 and LDR upon rapamycin stimulation resulted in global lamellipodial extensions (Fig. 4E,F). This discrepancy is presumably attributable to the difference of strength and duration in Rac1 activation between randomly migrating cells and cells expressing FKBP–Tiam1. Robust and sustained activation of Rac1 by the FKBP–Tiam1 translocation system might cause inactivation of MLCK through phosphorylation by PAK, which is a downstream effector of Rac1 (Sanders et al., 1999). However, it has been reported that PAK directly phosphorylates Ser19 of MLC and induces an increase in actomyosin contraction in endothelial cells (Chew et al., 1998; Zeng et al., 2000). Therefore, future studies will be needed to evaluate the spatial and temporal regulation of MLCK activity in migrating cells.

Evidence of a pathway from the actin cytoskeleton to Rac1 was provided by cross-correlation analysis (Fig. 3) and by the latrunculin-B-induced decrease of Rac1 activity (Fig. 4). In this context, we should note that Rac1 induces actin polymerization and formation of lamellipodia (Hall, 1998) (Fig. 4E,F). These

data indicate the existence of a positive feedback loop between the actin cytoskeleton and Rac1. Although it remains unknown how the actin cytoskeleton regulates Rac1 activity, we can adduce several mechanisms of the positive feedback loop. Some GEFs acting on Rac1, such as FGDs, Frabin (Nakanishi and Takai, 2008) and Asef2 (Sagara et al., 2009), interact with F-actin directly or indirectly. These GEFs are candidate molecules for a role in the positive feedback. Furthermore, focal complexes and adhesions induced by Rac1 at lamellipodia recruit the Cas–Crk–DOCK signaling complex (Côté and Vuori, 2007; Meller et al., 2005) and lead to the further activation of Rac1 in a manner consistent with the positive feedback. Such positive feedback regulation between PtdIns(3,4,5)P_3, Rac1 and actin has been well characterized in *Dictyostelium* cells, neutrophils and PC12 cells (Aoki et al., 2007; Iijima et al., 2002; Merlot and Firtel, 2003; Weiner et al., 2002). In contrast to these earlier works, PtdIns(3,4,5)P_3 was not involved in the positive feedback in the present model (Fig. 7). Consistent with this, Inoue et al. have shown with HL-60 neutrophils that rapid activation of endogenous Rac1 proteins triggers effective actin polymerization in the absence of PI3K activation and increase in PtdIns(3,4,5)P_3 (Inoue and Meyer, 2008).

Cross-correlation analyses have been applied to understand how Rho GTPases coordinate the morphodynamics (Machacek et al., 2009; Tsukada et al., 2008). Tsukada et al. have demonstrated, using the edge evolution tracking (EET) method, that the change in cell edge velocity precedes the activation of Rac1 and Cdc42, with a time delay of ~6 and 8 minutes, respectively (Tsukada et al., 2008). By contrast, Machacek et al. have shown with a sophisticated image processing technique that Cdc42 and Rac1 are activated ~40 seconds after the increase in the edge velocity (Machacek et al., 2009). Differences in the values of the time delay between these studies and our study, 2.2 minutes for Rac1, could arise from two reasons: the differences in image processing algorithms, and the use or not of a classification system for the modes of cell migration. With respect to the first reason, Machacek et al. analyzed the local area of the cell periphery, i.e. only the protrusive area, with image sets acquired for a shorter time interval of 10 seconds than ours of 1 minute. We, instead, focused on the global membrane dynamics of protrusion and retraction in the entire cell periphery of migrating HT-1080 cells. This could cause larger time delay values than those obtained in Machacek's study. With respect to the second reason, we classified the modes of cell migration into four categories – wave-like, oscillatory, directional and unclassifiable – and analyzed only the cells that were categorized into the wave-like migration. By contrast, Tsukada et al. did not use any categorization. Time-delay values obtained from directionally migrating cells became much greater than those of the cells migrating in the other modes. Therefore, the use of classification resulted in shorter delay timing in our study than Tsukada's studies (Tsukada et al., 2008). Notably, we assumed that the proposed feedback regulations between Rac1, actin cytoskeleton and MLCK took place in both protrusions and retractions in migrating HT-1080 cells for the following reasons. (1) Data obtained from cross-correlation analysis at the front of migrating cells contributed to the total correlation coefficient value to a similar extent as that obtained at the back of migrating cells. (2) We did not recognize any difference in the correlative relationship of Rac1 or Cdc42 activities and edge velocity between the front and back of cell movements; namely, at the front, increase in edge velocity preceded increase in Rac1 activity, whereas, at the back, decrease in edge velocity preceded decrease in Rac1 activity. It was also noted that a correlation-based multiplexing approach should be carefully applied to a system with feedback interactions (Sabouri-Ghomi et al., 2008). In our study the delay timing obtained by correlation analysis was within 2.2 minutes for Rac1 (Fig. 3); whereas, the effect of feedback regulation appeared at 4–6 minutes later (Fig. 6). Thus, it is unlikely that the feedback regulation interferes with the correlation analysis.

By employing image processing, statistical analysis and pharmacological perturbations, this study has demonstrated the molecular mechanisms underlying the ordered membrane dynamics in randomly migrating eukaryotic cells. A pivotal question to be answered is what factors initiate the increase in edge velocity prior to Rac1 activation. Our data showed that PtdIns(3,4,5)P_3 accumulated concomitantly with the increase in edge velocity (Fig. 3). Additionally, it has been recently reported that membrane curvature induces actin polymerization through EFC and/or F-BAR proteins and the N-WASP–WIP complex (Takano et al., 2008). In line with this finding, maximal F-actin assembly was observed ~20 seconds after maximal edge advancement (Ji et al., 2008). These results suggest the involvement of lipid regulation, which serves as a trigger for membrane protrusion. Further studies will be needed to uncover the molecular mechanism of the dynamics in migratory cells.

Materials and Methods

FRET biosensors
The plasmids encoding FRET biosensors have been described as follows: Raichu-Rac1/1011x, pRaichu-Cdc42/1054x (Itoh et al., 2002), pRaichu-RhoA/1294x (Nakamura et al., 2005; Yoshizaki et al., 2003), pPippi-PtdIns(3,4,5)P_3/1747x, pPippi-PtdIns(3,4)P_2/1759X (Aoki et al., 2005; Sato et al., 2003), pPippi-PtdIns(4,5)P_2/1758X (Nishioka et al., 2008) and pRaichu-Pak-Rho/1110x, a negative control (Kurokawa and Matsuda, 2005).

Cells, plasmids and reagents
HT-1080 cells were purchased from the American Type Culture Collection or the Japan Cell Resource Bank, and maintained in DMEM (Sigma-Aldrich, St. Louis, MO) supplemented with 10% fetal bovine serum (FBS). The cells were plated on 35-mm glass-bottomed dishes (Asahi Techno Glass, Tokyo, Japan), which were pre-coated with collagen type I (Nitta Gelatin Inc., Osaka, Japan). Plasmids were transfected into HT-1080 cells with Lipofectamine 2000 according to the manufacturer's protocol (Invitrogen, San Diego, CA). cDNA of Lifeact, a 17-amino-acid peptide (Riedl et al., 2008), were subcloned into the pCAGGS-EGFP vector. EGFP–Long-MLCK was a kind gift from Anne R. Bresnick (Poperechnaya et al., 2000). Expression plasmids for ERed–NES, LDR (Lyn11-targeted FRB), FKBP and FKBP–Tiam1 have been described previously (Aoki et al., 2007; Inoue et al., 2005). cDNA for FKBP–iSH2 was subcloned into pCAGGS-GST vector to obtain pCAGGS-GST-FKBP-iSH2 (Inoue and Meyer, 2008). LY294002 were obtained from Sigma-Aldrich (St. Louis, MO). Latrunculin B, cytochalasin D, ML-7 and Y27632 were purchased from Calbiochem (La Jolla, CA). PIK-93, which is a PI3K inhibitor, was obtained from Symansis NZ (Timaru, New Zealand). Rapamycin was purchased from LC Laboratories (Woburn, MA).

Time-lapse FRET imaging
FRET imaging was done essentially as previously described (Aoki and Matsuda, 2009). Briefly, HT-1080 cells expressing biosensors were suspended in trypsin, plated on collagen-coated 35-mm glass-bottomed dishes, and left for approximately 1 hour. At the time that cells were being plated, the culture medium was replaced with Phenol-Red-free DMEM/F12 containing 10% FBS, and overlaid with mineral oil to prevent evaporation. Cells were imaged with an inverted microscope (IX81; Olympus, Tokyo, Japan) equipped with a 60× objective lens (Olympus), a cooled CCD camera (Cool SNAP-K4; Roper Scientific), an LED illumination system (CoolLED precisExcite; Molecular Devices), an IX2-ZDC laser-based autofocusing system (Olympus) and an MD-XY30100T-Meta automatically programmable XY stage (Sigma Koki, Tokyo, Japan). The following filters were used for the dual emission imaging studies: excitation filters, 435/20 for CFP and FRET (Olympus), S492/18x for GFP (Chroma) and 580AF20 for RFP (Omega Optical, Brattleboro, VT); dichroic mirrors, XF2034 for CFP and FRET (Omega) and 86006bs for GFP and RFP

(Chroma); emission filters, 480AF30 for CFP (Omega), 535AF26 for FRET and GFP (Omega) and 635DF55 for RFP (Omega). The exposure time was 400 mseconds for CFP and FRET images when the binning was set to 4×4. After background subtraction, FRET/CFP ratio images were created with MetaMorph software (Universal Imaging, West Chester, PA), and represented by the intensity modulated display mode. In the intensity-modulated display mode, eight colors, from red to blue, are used to represent the FRET/CFP ratio, with the intensity of each color indicating the average intensity of FRET and CFP.

Mapping of velocity and molecular activity in the leading edge

The velocity of the leading edge in migrating HT-1080 cells was calculated using a mechanical model with some modifications (Machacek and Danuser, 2006). The process was divided into two steps: (1) image processing and (2) velocity calculating.

(1) Image processing. First, FRET or GFP images were binarized by the threshold value, which was determined arbitrarily to identify the cell edge (supplementary material Fig. S1A,B). Second, an Erode operation was applied to the binarized images three times to reduce the noise of the periphery (supplementary material Fig. S1C). Third, the outline of the eroded images was captured by line scanning to correct the data of the two-dimensional coordinates and FRET/CFP ratio values of the cell periphery (supplementary material Fig. S1D). These processes were implemented using MetaMorph software (Universal Imaging). There was no use of interior positions, only the edge positions.

(2) Velocity calculating. First, the data of the XY coordinates and FRET/CFP ratio values, which were obtained by the image processing, were normalized to 200 sampling windows. Second, to quantify the edge velocity, the window that was located at an angle of 0° from the centroid was set as an initial point (Fig. 2A). Third, normal vectors were obtained along the cell boundary (supplementary material Fig. S1E). Normal vector angles were affected especially in the region with strong boundary deformation (Machacek and Danuser, 2006). Therefore, fourth, the normal vector angles were corrected by averaging angles of five backward and five forward vectors (supplementary material Fig. S1F). Lastly, by using the averaged vectors, the boundary displacement at the time T was obtained by calculating the minimum distance from the point at time T to the point at time $T+1$, and divided by the interval time of imaging to obtain the edge velocity (supplementary material Fig. S1G). We denoted the matrices of edge velocity and molecular activity/localization as $\{M(x,t)|0 \leq x \leq 200, \ 0 \leq t\}$ and $\{F(x,t)|0 \leq x \leq 200, \ 0 \leq t\}$, respectively, where M is spatio-temporal data of morphological changes and F is spatio-temporal data of molecular activity or molecular localization. These processes were implemented using Matlab software (version R2010b; The Mathworks Inc., Natick, MA).

Correlation analysis

The auto- and cross-correlation analysis was performed essentially as described previously (Maeda et al., 2008). The auto-correlation functions of $M(x,t)$ and $F(x,t)$, and the cross-correlation function between $M(x,t)$ and $F(x,t)$ are defined as:

$$ACF(\Delta x, \Delta t) \equiv \frac{\langle (M(x+\Delta x, t+\Delta t) - M_{ave})(M(x,t) - M_{ave}) \rangle_{x,t}}{\langle (M(x,t) - M_{ave})^2 \rangle_{x,t}}$$

$$CCF(\Delta x, \Delta t) \equiv \frac{\langle (M(x+\Delta x, t+\Delta t) - M_{ave})(F(x,t) - F_{ave}) \rangle_{x,t}}{\langle (M(x,) - M_{ave})^2 \rangle_{x,t}^{\frac{1}{2}} \langle (F(x,t) - F_{ave})^2 \rangle_{x,t}^{\frac{1}{2}}},$$

where the numbers M_{ave} and F_{ave} indicate the average value of $M(x,t)$ and $F(x,t)$, respectively. The operator $\langle \rangle_{x,t}$ denotes the averages over time and over space. The range of calculation is the entire period of measurement in time and space from 0 to 200. Correlation analyses were implemented using Matlab software.

Classification of migration pattern

Random migration patterns of HT-1080 cells, i.e. wave-like, oscillatory, directional, and non-classifiable migration, were categorized on the basis of the ordered pattern of auto-correlation function in edge velocity, as shown in Fig. 2F. First, non-classifiable disordered pattern of the auto-correlation function was discriminated from the other migration patterns. Then, directional migration was classified as a value of $\Delta t_0 > 30$ minutes defined as a threshold criteria in the temporal auto-correlation function (ΔSpace=0, dashed line in Fig. 2D). Finally, wave-like migration was distinguished from oscillatory migration by the typical wavy shapes in the auto-correlation function.

Modeling and numerical simulation

All kinetic reactions in Models A–D (Fig. 5) were described by ordinary differential equations based on Michaelis–Menten kinetics. Equations and parameters in Models A to D are listed in supplementary material Tables S2–S5, respectively. Numerical simulation was performed using Matlab software. To achieve the adaptation, we assumed one constraint: the reaction rates and Michaelis constants of the buffering node (k_{node} and $K_{m \ node}$) were set to smaller

values than those of their substrate in order to saturate their reaction rates (Ma et al., 2009).

Supplementary material available online at
http://jcs.biologists.org/lookup/suppl/doi:10.1242/jcs.096859/-/DC1

References

Aoki, K. and Matsuda, M. (2009). Visualization of small GTPase activity with fluorescence resonance energy transfer-based biosensors. *Nat. Protoc.* **4**, 1623-1631.

Aoki, K., Nakamura, T., Fujikawa, K. and Matsuda, M. (2005). Local phosphatidylinositol 3,4,5-trisphosphate accumulation recruits Vav2 and Vav3 to activate Rac1/Cdc42 and initiate neurite outgrowth in nerve growth factor-stimulated PC12 cells. *Mol. Biol. Cell* **16**, 2207-2217.

Aoki, K., Nakamura, T., Inoue, T., Meyer, T. and Matsuda, M. (2007). An essential role for the SHIP2-dependent negative feedback loop in neuritogenesis of nerve growth factor-stimulated PC12 cells. *J. Cell Biol.* **177**, 817-827.

Aoki, K., Kiyokawa, E., Nakamura, T. and Matsuda, M. (2008). Visualization of growth signal transduction cascades in living cells with genetically encoded probes based on Förster resonance energy transfer. *Philos. Trans. R. Soc. Lond. B Biol. Sci.* **363**, 2143-2151.

Arai, Y., Shibata, T., Matsuoka, S., Sato, M. J., Yanagida, T. and Ueda, M. (2010). Self-organization of the phosphatidylinositol lipids signaling system for random cell migration. *Proc. Natl. Acad. Sci. USA* **107**, 12399-12404.

Chew, T. L., Masaracchia, R. A., Goeckeler, Z. M. and Wysolmerski, R. B. (1998). Phosphorylation of non-muscle myosin II regulatory light chain by p21-activated kinase (gamma-PAK). *J. Muscle Res. Cell Motil.* **19**, 839-854.

Coates, T. D., Watts, R. G., Hartman, R. and Howard, T. H. (1992). Relationship of F-actin distribution to development of polar shape in human polymorphonuclear neutrophils. *J. Cell Biol.* **117**, 765-774.

Côté, J. F. and Vuori, K. (2007). GEF what? Dock180 and related proteins help Rac to polarize cells in new ways. *Trends Cell Biol.* **17**, 383-393.

Dewitt, S., Darley, R. L. and Hallett, M. B. (2009). Translocation or just location? Pseudopodia affect fluorescent signals. *J. Cell Biol.* **184**, 197-203.

Döbereiner, H. G., Dubin-Thaler, B. J., Hofman, J. M., Xenias, H. S., Sims, T. N., Giannone, G., Dustin, M. L., Wiggins, C. H. and Sheetz, M. P. (2006). Lateral membrane waves constitute a universal dynamic pattern of motile cells. *Phys. Rev. Lett.* **97**, 038102.

Giannone, G., Dubin-Thaler, B. J., Döbereiner, H. G., Kieffer, N., Bresnick, A. R. and Sheetz, M. P. (2004). Periodic lamellipodial contractions correlate with rearward actin waves. *Cell* **116**, 431-443.

Gierer, A. and Meinhardt, H. (1972). A theory of biological pattern formation. *Kybernetik* **12**, 30-39.

Hall, A. (1998). Rho GTPases and the actin cytoskeleton. *Science* **279**, 509-514.

Hoffman, R. M. (2005). The multiple uses of fluorescent proteins to visualize cancer in vivo. *Nat. Rev. Cancer* **5**, 796-806.

Iijima, M., Huang, Y. E. and Devreotes, P. (2002). Temporal and spatial regulation of chemotaxis. *Dev. Cell* **3**, 469-478.

Inoue, T. and Meyer, T. (2008). Synthetic activation of endogenous PI3K and Rac identifies an AND-gate switch for cell polarization and migration. *PLoS ONE* **3**, e3068.

Inoue, T., Heo, W. D., Grimley, J. S., Wandless, T. J. and Meyer, T. (2005). An inducible translocation strategy to rapidly activate and inhibit small GTPase signaling pathways. *Nat. Methods* **2**, 415-418.

Itoh, R. E., Kurokawa, K., Ohba, Y., Yoshizaki, H., Mochizuki, N. and Matsuda, M. (2002). Activation of rac and cdc42 video imaged by fluorescent resonance energy transfer-based single-molecule probes in the membrane of living cells. *Mol. Cell. Biol.* **22**, 6582-6591.

Ji, L., Lim, J. and Danuser, G. (2008). Fluctuations of intracellular forces during cell protrusion. *Nat. Cell Biol.* **10**, 1393-1400.

Knight, Z. A., Gonzalez, B., Feldman, M. E., Zunder, E. R., Goldenberg, D. D., Williams, O., Loewith, R., Stokoe, D., Balla, A., Toth, B. et al. (2006). A pharmacological map of the PI3-K family defines a role for p110α in insulin signaling. *Cell* **125**, 733-747.

Kondo, S. and Miura, T. (2010). Reaction-diffusion model as a framework for understanding biological pattern formation. *Science* **329**, 1616-1620.

Kraynov, V. S., Chamberlain, C., Bokoch, G. M., Schwartz, M. A., Slabaugh, S. and Hahn, K. M. (2000). Localized Rac activation dynamics visualized in living cells. *Science* **290**, 333-337.

Kudryashov, D. S., Chibalina, M. V., Birukov, K. G., Lukas, T. J., Sellers, J. R., Van Eldik, L. J., Watterson, D. M. and Shirinsky, V. P. (1999). Unique sequence of a high molecular weight myosin light chain kinase is involved in interaction with actin cytoskeleton. *FEBS Lett.* **463**, 67-71.

Kurokawa, K. and Matsuda, M. (2005). Localized RhoA activation as a requirement for the induction of membrane ruffling. *Mol. Biol. Cell* **16**, 4294-4303.

Kurokawa, K., Itoh, R. E., Yoshizaki, H., Nakamura, Y. O. and Matsuda, M. (2004). Coactivation of Rac1 and Cdc42 at lamellipodia and membrane ruffles induced by epidermal growth factor. *Mol. Biol. Cell* **15**, 1003-1010.

Lauffenburger, D. A. and Horwitz, A. F. (1996). Cell migration: a physically integrated molecular process. *Cell* **84**, 359-369.

Ma, W., Trusina, A., El-Samad, H., Lim, W. A. and Tang, C. (2009). Defining network topologies that can achieve biochemical adaptation. *Cell* **138**, 760-773.

Machacek, M. and Danuser, G. (2006). Morphodynamic profiling of protrusion phenotypes. *Biophys. J.* **90**, 1439-1452.

Machacek, M., Hodgson, L., Welch, C., Elliott, H., Pertz, O., Nalbant, P., Abell, A., Johnson, G. L., Hahn, K. M. and Danuser, G. (2009). Coordination of Rho GTPase activities during cell protrusion. *Nature* **461**, 99-103.

Maeda, Y. T., Inose, J., Matsuo, M. Y., Iwaya, S. and Sano, M. (2008). Ordered patterns of cell shape and orientational correlation during spontaneous cell migration. *PLoS ONE* **3**, e3734.

Meller, N., Merlot, S. and Guda, C. (2005). CZH proteins: a new family of Rho-GEFs. *J. Cell Sci.* **118**, 4937-4946.

Merlot, S. and Firtel, R. A. (2003). Leading the way: directional sensing through phosphatidylinositol 3-kinase and other signaling pathways. *J. Cell Sci.* **116**, 3471-3478.

Mitchison, T. J. and Cramer, L. P. (1996). Actin-based cell motility and cell locomotion. *Cell* **84**, 371-379.

Miyawaki, A. (2003). Visualization of the spatial and temporal dynamics of intracellular signaling. *Dev. Cell* **4**, 295-305.

Nakamura, T., Aoki, K. and Matsuda, M. (2005). FRET imaging in nerve growth cones reveals a high level of RhoA activity within the peripheral domain. *Brain Res. Mol. Brain Res.* **139**, 277-287.

Nakanishi, H. and Takai, Y. (2008). Phenomenin Review Series: Frabin and other related Cdc42-specific guanine nucleotide exchange factors couple the actin cytoskeleton with the plasma membrane. *J. Cell. Mol. Med.* **12**, 1169-1176.

Nalbant, P., Hodgson, L., Kraynov, V., Toutchkine, A. and Hahn, K. M. (2004). Activation of endogenous Cdc42 visualized in living cells. *Science* **305**, 1615-1619.

Niggli, V., Schmid, M. and Nievergelt, A. (2006). Differential roles of Rho-kinase and myosin light chain kinase in regulating shape, adhesion, and migration of HT1080 fibrosarcoma cells. *Biochem. Biophys. Res. Commun.* **343**, 602-608.

Nishioka, T., Aoki, K., Hikake, K., Yoshizaki, H., Kiyokawa, E. and Matsuda, M. (2008). Rapid turnover rate of phosphoinositides at the front of migrating MDCK cells. *Mol. Biol. Cell* **19**, 4213-4223.

Otsuji, M., Terashima, Y., Ishihara, S., Kuroda, S. and Matsushima, K. (2010). A conceptual molecular network for chemotactic behaviors characterized by feedback of molecules cycling between the membrane and the cytosol. *Sci. Signal.* **3**, ra89.

Pertz, O., Hodgson, L., Klemke, R. L. and Hahn, K. M. (2006). Spatiotemporal dynamics of RhoA activity in migrating cells. *Nature* **440**, 1069-1072.

Peyrollier, K., Hajduch, E., Gray, A., Litherland, G. J., Prescott, A. R., Leslie, N. R. and Hundal, H. S. (2000). A role for the actin cytoskeleton in the hormonal and growth-factor-mediated activation of protein kinase B. *Biochem. J.* **352**, 617-622.

Poperechnaya, A., Varlamova, O., Lin, P. J., Stull, J. T. and Bresnick, A. R. (2000). Localization and activity of myosin light chain kinase isoforms during the cell cycle. *J. Cell Biol.* **151**, 697-708.

Rajakulendran, T., Sahmi, M., Lefrançois, M., Sicheri, F. and Therrien, M. (2009). A dimerization-dependent mechanism drives RAF catalytic activation. *Nature* **461**, 542-545.

Ridley, A. J. (2001). Rho GTPases and cell migration. *J. Cell Sci.* **114**, 2713-2722.

Riedl, J., Crevenna, A. H., Kessenbrock, K., Yu, J. H., Neukirchen, D., Bista, M., Bradke, F., Jenne, D., Holak, T. A., Werb, Z. et al. (2008). Lifeact: a versatile marker to visualize F-actin. *Nat. Methods* **5**, 605-607.

Saarikangas, J., Zhao, H. and Lappalainen, P. (2010). Regulation of the actin cytoskeleton-plasma membrane interplay by phosphoinositides. *Physiol. Rev.* **90**, 259-289.

Sabouri-Ghomi, M., Wu, Y., Hahn, K. and Danuser, G. (2008). Visualizing and quantifying adhesive signals. *Curr. Opin. Cell Biol.* **20**, 541-550.

Sagara, M., Kawasaki, Y., Iemura, S. I., Natsume, T., Takai, Y. and Akiyama, T. (2009). Asef2 and Neurabin2 cooperatively regulate actin cytoskeletal organization and are involved in HGF-induced cell migration. *Oncogene* **28**, 1357-1365.

Sanders, L. C., Matsumura, F., Bokoch, G. M. and de Lanerolle, P. (1999). Inhibition of myosin light chain kinase by p21-activated kinase. *Science* **283**, 2083-2085.

Sato, M., Ueda, Y., Takagi, T. and Umezawa, Y. (2003). Production of PtdInsP3 at endomembranes is triggered by receptor endocytosis. *Nat. Cell Biol.* **5**, 1016-1022.

Schmidt, A. and Hall, A. (2002). Guanine nucleotide exchange factors for Rho GTPases: turning on the switch. *Genes Dev.* **16**, 1587-1609.

Smith, L., Parizi-Robinson, M., Zhu, M. S., Zhi, G., Fukui, R., Kamm, K. E. and Stull, J. T. (2002). Properties of long myosin light chain kinase binding to F-actin in vitro and in vivo. *J. Biol. Chem.* **277**, 35597-35604.

Srinivasan, S., Wang, F., Glavas, S., Ott, A., Hofmann, F., Aktories, K., Kalman, D. and Bourne, H. R. (2003). Rac and Cdc42 play distinct roles in regulating PI(3,4,5)P3 and polarity during neutrophil chemotaxis. *J. Cell Biol.* **160**, 375-385.

Takano, K., Toyooka, K. and Suetsugu, S. (2008). EFC/F-BAR proteins and the N-WASP-WIP complex induce membrane curvature-dependent actin polymerization. *EMBO J.* **27**, 2817-2828.

Totsukawa, G., Wu, Y., Sasaki, Y., Hartshorne, D. J., Yamakita, Y., Yamashiro, S. and Matsumura, F. (2004). Distinct roles of MLCK and ROCK in the regulation of membrane protrusions and focal adhesion dynamics during cell migration of fibroblasts. *J. Cell Biol.* **164**, 427-439.

Tsukada, Y., Aoki, K., Nakamura, T., Sakumura, Y., Matsuda, M. and Ishii, S. (2008). Quantification of local morphodynamics and local GTPase activity by edge evolution tracking. *PLOS Comput. Biol.* **4**, e1000223.

Wang, F., Herzmark, P., Weiner, O. D., Srinivasan, S., Servant, G. and Bourne, H. R. (2002). Lipid products of PI(3)Ks maintain persistent cell polarity and directed motility in neutrophils. *Nat. Cell Biol.* **4**, 513-518.

Weiner, O. D., Neilsen, P. O., Prestwich, G. D., Kirschner, M. W., Cantley, L. C. and Bourne, H. R. (2002). A PtdInsP(3)- and Rho GTPase-mediated positive feedback loop regulates neutrophil polarity. *Nat. Cell Biol.* **4**, 509-513.

Weiner, O. D., Marganski, W. A., Wu, L. F., Altschuler, S. J. and Kirschner, M. W. (2007). An actin-based wave generator organizes cell motility. *PLoS Biol.* **5**, e221.

Yoshizaki, H., Ohba, Y., Kurokawa, K., Itoh, R. E., Nakamura, T., Mochizuki, N., Nagashima, K. and Matsuda, M. (2003). Activity of Rho-family GTPases during cell division as visualized with FRET-based probes. *J. Cell Biol.* **162**, 223-232.

Zeng, Q., Lagunoff, D., Masaracchia, R., Goeckeler, Z., Côté, G. and Wysolmerski, R. (2000). Endothelial cell retraction is induced by PAK2 monophosphorylation of myosin II. *J. Cell Sci.* **113**, 471-482.